Constructing higher order discontinuity-capturing schemes with upwind-biased interpolations and boundary variation diminishing algorithm

Xi Deng, Yuya Shimizu, Bin Xie, Feng Xiao

Version of Record: https://www.sciencedirect.com/science/article/pii/S0045793020300098
Manuscript_bc9b458199618133f08a95f62984ebc3

Constructing higher order discontinuity-capturing schemes with upwind-biased interpolations and boundary variation diminishing algorithm

Xi Deng[a,b,c,*], Yuya Shimizu[c], Bin Xie[d], Feng Xiao[c,*]

[a]*Aix Marseille Univ, CNRS, Centrale Marseille, M2P2, Marseille, France.*
[b]*Department of Aeronautics,Imperial College London,SW72 AZ, United Kingdom.*
[c]*Department of Mechanical Engineering, Tokyo Institute of Technology, 2-12-1 Ookayama, Meguro-ku, Tokyo, Japan.*
[d]*School of Naval Architecture, Department of Ocean and Civil Engineering, Shanghai Jiaotong University, Shanghai, 200240, China.*

Abstract

Based on the fifth-order scheme in our previous work (Deng et. al (2019) [28]), a new framework of constructing very high order discontinuity-capturing schemes is proposed for finite volume method. These schemes, so-called P_nT_m − BVD (polynomial of n-degree and THINC function of m-level reconstruction based on BVD algorithm), are designed by employing high-order upwind-biased interpolations and THINC (Tangent of Hyperbola for INterface Capturing) functions with adaptive steepness as the reconstruction candidates. The final reconstruction function in each cell is determined with a multi-stage BVD (Boundary Variation Diminishing) algorithm so as to effectively control numerical oscillation and dissipation. We devise the new schemes up to eleventh order in an efficient way by directly increasing the order of the underlying upwind scheme using high order polynomials. The analysis of the spectral property and accuracy tests show that the new reconstruction strategy well preserves the low-dissipation property of the underlying upwind schemes with high-order polynomials for smooth solution over all wave numbers and realizes $n + 1$ order convergence rate. The performance of new schemes is examined through widely used benchmark tests, which demonstrate that the proposed schemes are capable of simultaneously resolving small-scale flow features with high resolution and capturing discontinuities with low dissipation. With outperforming results and simplicity in algorithm, the new reconstruction strategy shows great potential as an alternative numerical framework for computing nonlinear hyperbolic conservation laws that have discontinuous and smooth solutions of different scales.

Keywords: shock capturing, very high order schemes, boundary variation diminishing

1. Introduction

Designing shock-capturing schemes for high speed compressible flows involving complex flow structures of wide range scales still remains an unresolved issue and attracts a lot of attention in the computational fluid dynamics community. The coexistence of discontinuities and small-scale flow features poses a big challenge to existing numerical

*Corresponding author: Dr. X. Deng (Email: deng.xi98@gmail.com) Dr. F. Xiao (Email: xiao.f.aa@m.titech.ac.jp)

schemes. High order and low dissipative schemes are demanded to resolve high-frequency waves and vortices featured in turbulent flows. However, high order schemes may cause spurious numerical oscillations when solving discontinuities such as shock waves, contacts and material interfaces. With the order increased, a scheme may become less robust or too oscillatory to use. To suppress numerical oscillations associated with high order interpolation, a common practice is to introduce certain amount of numerical dissipations by projecting high order interpolation polynomials to lower order or smoother ones, which is also known as limiting projection. An ideal limiting projection is expected to have as small as possible numerical dissipation, while still to effectively suppress numerical oscillation around critical regions. Excessive numerical dissipation introduced in limiting processes tends to undermine the accuracy even though high order interpolation is employed.

Over the decades, a great deal of efforts has been made to construct high order shock capturing schemes in finite volume or finite difference framework. Some representative methodologies to design shock capturing schemes are TVD (Total Variation Diminishing) [1, 2], ENO (Essentially Non-oscillatory) [3, 4, 5, 6], WENO (Weighted Essentially Non-oscillatory) [7, 8] and MOOD (Multi-dimensional Optimal Order Detection) method [9, 10, 11]. Among these schemes, the WENO family which is built on a weighted average of approximations from all candidate stencils is supposed to be one of widely-used methods. Lots of contributions have been made so far to improve the performance of the original WENO scheme. For example, it has been recognized that the classical WENO scheme generates excessive numerical dissipation that tends to smear out contact discontinuities or jumps in variables across material interface. Thus, a series of new smoothness indicators have been proposed in [12, 13, 14, 15, 16] where contributions of the less smooth candidate stencils are optimized to reduce numerical dissipation. Moreover, it is observed that the spectral property of the WENO schemes is inferior to that of low-dissipation linear scheme with high-order polynomials. Some recent efforts have been made to improve the spectral property of the WENO schemes. In [19], a new design strategy named embedded WENO is devised to utilise all adjacent smooth substencils to construct a desirable interpolation thus to improve the behavior of the spectral property. In spite of these works, there are still at least three remaining issues in existing high order shock-capturing schemes which need further investigations.

(1) In the vicinity of discontinuities the intrinsic numerical dissipation still persists and pollutes the numerical solution. The resolution of physical features such as contact surfaces, shear waves and material interfaces will evolve from bad to worse. To obtain a sharp discontinuous solution without numerical oscillations is challenging for any limiting processes.

(2) The limiting processes may regard high gradients and small-scale flow structures as discontinuities. Excessive use of limiting processes will undermine the accuracy and make the spectral property of designed schemes inferior to that of low-dissipation linear scheme. Especially, small-scale flow features in turbulence will be

smeared out by falsely triggered limiting processes.

(3) Extension schemes to very high order in finite volume or finite difference method may not be efficient and economical. As stated in [20, 21, 22], the WENO schemes involve more sub-stencils with increasing order. To evaluate the smoothness indicators is computationally expensive. Moreover, schemes may be less robust as order is increased. For example, there is a possibility of nonexistence of a smooth stencil when using higher-order schemes since the stencils used by the higher-order WENO schemes are quite large. Thus, in [21, 23] a recursive-order-reduction procedure is further adopted to suppress numerical oscillations when using higher-order WENO schemes.

We have recently developed a new class of shock-capturing schemes [24, 25, 26, 27, 28] which hybrid polynomial based nonlinear reconstructions and the THINC (Tangent of Hyperbola for INterface Capturing) function as the reconstruction candidates. Realizing that polynomial-based reconstruction may not be suitable for discontinuities, in [24] a non-polynomial jump-like THINC function is employed to represent the discontinuity. The switch between WENO and THINC is guided by the BVD (Boundary Variation Diminishing) algorithms, which select reconstruction functions by minimizing the jumps of the reconstructed values at the cell boundaries. The spectral analysis and numerical experiments [27] reveal that THINC function with properly chosen steepness can outperform most existing MUSCL schemes for spatial reconstruction. A new scheme, the adaptive THINC-BVD scheme, was then designed under the BVD principle by employing THINC functions with different sharpnesses to solve both smooth and discontinuous solutions [27]. Since THINC is a monotonic and bounded function, the adaptive THINC-BVD scheme is able to eliminate numerical oscillation without any limiting projection. For better use of the numerical property of the high order polynomial function, a fifth-order scheme is devised by employing a linear fifth-order upwind scheme and THINC function with the BVD algorithm in our most recent work [28]. The resulting scheme can retrieve linear upwind scheme in smooth region and capture sharp discontinuities without numerical oscillations. Our practice so far shows that the BVD principle can be used as a general and effective paradigm to design new numerical schemes.

In this paper, we propose a new general framework to construct high order shock capture scheme. These schemes, so-called $\mathrm{P}_n\mathrm{T}_m$ − BVD (polynomial of n-degree and THINC function of m-level reconstruction based on BVD algorithm), are designed by employing $n+1$ order upwind schemes with high order polynomials and THINC (Tangent of Hyperbola for INterface Capturing) functions with adaptive steepness as reconstruction candidates. The final reconstruction function in each cell is determined with multi-stage BVD (Boundary Variation Diminishing) algorithm so as to effectively control numerical oscillation and dissipation. As shown later in the paper, the proposed $\mathrm{P}_n\mathrm{T}_m$ − BVD schemes have following desirable properties: 1) they solve sharp discontinuities with effectively suppressed numerical oscillations; 2) they retrieve the underlying linear high-order schemes for smooth solution over all wave numbers, and

thus substantially reduce numerical dissipation errors for small-scale flow structures; 3) they can be extended to high order in an efficient way by simply increasing the order of the underlying upwind scheme.

The remainder of this paper is organized as follows. In Section 2, after a brief review of the finite volume method, the details of the new scheme for spatial reconstruction are presented. The spectral property of the new scheme will also be presented. In Section 3, the performance of the new scheme will be examined through benchmark tests in 1D and 2D. Some concluding remarks and prospective are given in Section 4.

2. Numerical methods

2.1. Finite volume method

In this paper, the 1D scalar conservation law in following form is used to introduce the new scheme

$$\frac{\partial q}{\partial t} + \frac{\partial f(q)}{\partial x} = 0, \tag{1}$$

where $q(x,t)$ is the solution function and $f(q)$ is the flux function. We divide the computational domain into N non-overlapping cell elements, $\mathcal{I}_i : x \in [x_{i-1/2}, x_{i+1/2}]$, $i = 1, 2, \ldots, N$, with a uniform grid spacing $h = \Delta x = x_{i+1/2} - x_{i-1/2}$. For a standard finite volume method, the volume-integrated average value $\bar{q}_i(t)$ in cell $\mathcal{I}_i$ is defined as

$$\bar{q}_i(t) \approx \frac{1}{\Delta x} \int_{x_{i-1/2}}^{x_{i+1/2}} q(x,t)\, dx. \tag{2}$$

The semi-discrete version of Eq. (1) in the finite volume form can be expressed as an ordinary differential equation (ODE)

$$\frac{\partial \bar{q}(t)}{\partial t} = -\frac{1}{\Delta x}(\tilde{f}_{i+1/2} - \tilde{f}_{i-1/2}), \tag{3}$$

where the numerical fluxes $\tilde{f}$ at cell boundaries can be computed by a Riemann solver

$$\tilde{f}_{i+1/2} = f^{\text{Riemann}}_{i+1/2}(q^L_{i+1/2}, q^R_{i+1/2}). \tag{4}$$

The remaining main task is how to calculate $q^L_{i+1/2}$ and $q^R_{i+1/2}$ through the reconstruction process.

2.2. Reconstruction process

In this subsection, we give the details of how to calculate $q^L_{i+1/2}$ and $q^R_{i+1/2}$ using the BVD principle. The proposed $\mathrm{P}_n\mathrm{T}_m$ − BVD schemes are designed by employing linear weight polynomial of n-degree and THINC function of m-level as the candidate interpolants. The final reconstruction function in each cell is selected from these candidate interpolants with the BVD algorithm. Next, we introduce the candidate interpolants before the description of the BVD algorithm.

2.2.1. Candidate interpolant P_n*: linear upwind scheme of n-degree polynomial*

A finite volume scheme of $(n+1)$th order can be constructed from a spatial approximation for the solution in the target cell $\mathcal{I}_i$ with a polynomial $\tilde{q}_i^{Pn}(x)$ of degree n. The $n+1$ unknown coefficients of the polynomial are determined by requiring that $\tilde{q}_i^{Pn}(x)$ has the same cell average on each cell over an appropriately selected stencil $S = \{i-n^-, \ldots, i+n^+\}$ with $n^- + n^+ = n$, which is expressed as

$$\frac{1}{\Delta x}\int_{x_{j-1/2}}^{x_{j+1/2}} \tilde{q}_i^{Pn}(x)dx = \bar{q}_j, \quad j = i-n^-, i-n^-+1, \ldots, i+n^+. \tag{5}$$

To construct $2r-1$ order upwind-biased (UW) finite volume schemes as detailed in [7, 8, 29], the stencil is defined with $n^- = n^+ = r-1$. The unknown coefficients of polynomial of $2r-2$ degree can be then calculated from (5). With the polynomial $\tilde{q}_i^{Pn}(x)$, high order approximation for reconstructed values at the cell boundaries can be obtained by

$$q_{i+\frac{1}{2}}^{L,Pn} = \tilde{q}_i^{Pn}(x_{i+\frac{1}{2}}) \text{ and } q_{i-\frac{1}{2}}^{R,Pn} = \tilde{q}_i^{Pn}(x_{i-\frac{1}{2}}). \tag{6}$$

The analysis of [7, 8, 29] shows that in smooth region, the approximation with polynomial (6) can achieve $2r-1$ order accuracy. In this work, we extend the proposed scheme from fifth order ($r=3$) to eleventh order ($r=6$) by using polynomials of 4th, 6th, 8th and 10th degree as underlying scheme for smooth solution. In order to facilitate the implementation of the proposed method, we give the explicit formulas of $q_{i+1/2}^{L,Pn}$ and $q_{i-1/2}^{R,Pn}$ for (n+1)th-order scheme as follows,

- 5th-order scheme

$$\begin{aligned} q_{i+1/2}^{L,P4} &= \frac{1}{30}\bar{q}_{i-2} - \frac{13}{60}\bar{q}_{i-1} + \frac{47}{60}\bar{q}_i + \frac{9}{20}\bar{q}_{i+1} - \frac{1}{20}\bar{q}_{i+2}, \\ q_{i-1/2}^{R,P4} &= \frac{1}{30}\bar{q}_{i+2} - \frac{13}{60}\bar{q}_{i+1} + \frac{47}{60}\bar{q}_i + \frac{9}{20}\bar{q}_{i-1} - \frac{1}{20}\bar{q}_{i-2}. \end{aligned} \tag{7}$$

- 7th-order scheme

$$\begin{aligned} q_{i+1/2}^{L,P6} &= -\frac{1}{140}\bar{q}_{i-3} + \frac{5}{84}\bar{q}_{i-2} - \frac{101}{420}\bar{q}_{i-1} + \frac{319}{420}\bar{q}_i + \frac{107}{210}\bar{q}_{i+1} - \frac{19}{210}\bar{q}_{i+2} + \frac{1}{105}\bar{q}_{i+3}, \\ q_{i-1/2}^{R,P6} &= -\frac{1}{140}\bar{q}_{i+3} + \frac{5}{84}\bar{q}_{i+2} - \frac{101}{420}\bar{q}_{i+1} + \frac{319}{420}\bar{q}_i + \frac{107}{210}\bar{q}_{i-1} - \frac{19}{210}\bar{q}_{i-2} + \frac{1}{105}\bar{q}_{i-3}. \end{aligned} \tag{8}$$

- 9th-order scheme

$$\begin{aligned} q_{i+1/2}^{L,P8} &= \frac{1}{630}\bar{q}_{i-4} - \frac{41}{2520}\bar{q}_{i-3} + \frac{199}{2520}\bar{q}_{i-2} - \frac{641}{2520}\bar{q}_{i-1} + \frac{1879}{2520}\bar{q}_i + \frac{275}{504}\bar{q}_{i+1} - \frac{61}{504}\bar{q}_{i+2} + \frac{11}{501}\bar{q}_{i+3} - \frac{1}{504}\bar{q}_{i+4}, \\ q_{i-1/2}^{R,P8} &= \frac{1}{630}\bar{q}_{i+4} - \frac{41}{2520}\bar{q}_{i+3} + \frac{199}{2520}\bar{q}_{i+2} - \frac{641}{2520}\bar{q}_{i+1} + \frac{1879}{2520}\bar{q}_i + \frac{275}{504}\bar{q}_{i-1} - \frac{61}{504}\bar{q}_{i-2} + \frac{11}{501}\bar{q}_{i-3} - \frac{1}{504}\bar{q}_{i-4}. \end{aligned} \tag{9}$$

- 11th-order scheme

$$
\begin{aligned}
q_{i+1/2}^{L,P10} = & -\frac{1}{2772}\bar{q}_{i-5} + \frac{61}{13860}\bar{q}_{i-4} - \frac{703}{27720}\bar{q}_{i-3} + \frac{371}{3960}\bar{q}_{i-2} - \frac{7303}{27720}\bar{q}_{i-1} + \frac{20417}{27720}\bar{q}_{i} + \frac{15797}{27720}\bar{q}_{i+1} - \frac{4003}{27720}\bar{q}_{i+2} \\
& -\frac{947}{27720}\bar{q}_{i+3} + \frac{17}{3080}\bar{q}_{i+4} + \frac{1}{2310}\bar{q}_{i+5}, \\
q_{i-1/2}^{R,P10} = & -\frac{1}{2772}\bar{q}_{i+5} + \frac{61}{13860}\bar{q}_{i+4} - \frac{703}{27720}\bar{q}_{i+3} + \frac{371}{3960}\bar{q}_{i+2} - \frac{7303}{27720}\bar{q}_{i+1} + \frac{20417}{27720}\bar{q}_{i} + \frac{15797}{27720}\bar{q}_{i-1} - \frac{4003}{27720}\bar{q}_{i-2} \\
& -\frac{947}{27720}\bar{q}_{i-3} + \frac{17}{3080}\bar{q}_{i-4} + \frac{1}{2310}\bar{q}_{i-5}.
\end{aligned} \tag{10}
$$

2.2.2. Candidate interpolant T_m*: non-polynomial THINC function with m-level steepness*

Another candidate interpolation function in our scheme makes use of the THINC interpolation which is a differentiable and monotone Sigmoid function [30, 31]. The piecewise THINC reconstruction function is written as

$$
\tilde{q}_i^T(x) = \bar{q}_{min} + \frac{\bar{q}_{max}}{2}\left[1 + \theta\ \tanh\left(\beta\left(\frac{x - x_{i-1/2}}{x_{i+1/2} - x_{i-1/2}} - \tilde{x}_i\right)\right)\right], \tag{11}
$$

where $\bar{q}_{min} = \min(\bar{q}_{i-1}, \bar{q}_{i+1})$, $\bar{q}_{max} = \max(\bar{q}_{i-1}, \bar{q}_{i+1}) - \bar{q}_{min}$ and $\theta = sgn(\bar{q}_{i+1} - \bar{q}_{i-1})$. The jump thickness is controlled by the parameter β, i.e. a small value of β leads to a smooth profile while a large one leads to a sharp jump-like distribution. The unknown $\tilde{x}_i$, which represents the location of the jump center, is computed from constraint condition $\bar{q}_i = \dfrac{1}{\Delta x}\displaystyle\int_{x_{i-1/2}}^{x_{i+1/2}} \tilde{q}_i^T(x)dx$. More details about the property of THINC function can be referred in our previous work [27].

Following [27], in this work we use THINC functions with β of m different values to represent different steepness, to realize non-oscillatory and less-dissipative reconstructions adaptively for various flow structures. A THINC reconstruction function $\tilde{q}_i^{Tk}(x)$ with β_k gives the reconstructed values $q_{i+1/2}^{L,Tk}$ and $q_{i-1/2}^{R,Tk}$, $(k = 1, 2, \ldots, m)$. We will use m up to three in present study.

2.2.3. The BVD algorithm

The underlying high order upwind schemes (7)-(10) can achieve the targeted optimal order for smooth region. However, numerical oscillations will appear for discontinuous solutions, such as the shock waves in high speed compressible flow. As aforementioned, in the conventional high resolution schemes, nonlinear limiting projections are designed to suppress such numerical oscillations in presence of discontinuous solutions. Unfortunately, these limiting processes usually undermine the accuracy and can hardly retrieve the original high-order linear schemes for smooth solutions of relatively small scales. An ideal limiting projection should maintain as much as possible the numerical properties of the scheme that uses the original polynomial of linear weights. In this work, we present a novel reconstruction scheme based on the BVD principle, where the linear high order schemes are directly used for smooth solutions.

In [27], a variant BVD algorithm was devised to minimize the total boundary variation (TBV), which implies that the reconstruction function which fits better with the flow field distribution will give a smaller boundary variation value. Thus using monotonic interpolations results in smaller boundary variation values in presence of discontinuous solution, whereas high-order interpolations are preferred to minimize the boundary variations for smooth region. In the $\mathrm{P}_n\mathrm{T}_m$ − BVD schemes presented in this paper, reconstruction function is determined from the candidate interpolants with k-stage ($k = m$) BVD algorithm so as to minimize the TBV of the target cell. We denote the reconstruction function in the target cell $\mathcal{I}_i$ after the k-th stage BVD as $\tilde{q}_i^{<k>}(x)$.

The k-stage BVD algorithm is formulated as follows.

(I): Initial stage ($k = 0$)**:**

(I-I) As the first step, use the linear high-order upwind scheme as the base reconstruction scheme and initialize the reconstructed function as $\tilde{q}_i^{<0>}(x) = \tilde{q}_i^{Pn(x)}$.

(II) The intermediate BVD stage ($k = 1, \ldots, m-1$)**:**

(II-I) Set $\tilde{q}_i^{<k>}(x) = \tilde{q}_i^{<k-1>}(x)$

(II-II) Calculate the TBV values for target cell $\mathcal{I}_i$ from the reconstruction of $\tilde{q}_i^{<k>}(x)$

$$TBV_i^{<k>} = \left|q_{i-1/2}^{L,<k>} - q_{i-1/2}^{R,<k>}\right| + \left|q_{i+1/2}^{L,<k>} - q_{i+1/2}^{R,<k>}\right| \tag{12}$$

and from the THINC function $\tilde{q}_i^{Tk}(x)$ with a steepness β_k as

$$TBV_i^{Tk} = \left|q_{i-1/2}^{L,Tk} - q_{i-1/2}^{R,Tk}\right| + \left|q_{i+1/2}^{L,Tk} - q_{i+1/2}^{R,Tk}\right|. \tag{13}$$

(II-III) Modify the reconstruction function for cells $i-1$, i and $i+1$ according to the following BVD algorithm

$$\tilde{q}_j^{<k>}(x) = \tilde{q}_j^{Tk}(x), \;\; j = i-1, i, i+1; \quad \text{if} \;\; TBV_i^{Tk} < TBV_i^{<k>}. \tag{14}$$

(III) The final BVD stage ($k = m$)**:**

(III-I) Given the reconstruction functions $\tilde{q}_i^{<m-1>}(x)$ from above stage, compute the TBV using the reconstructed cell boundary values from previous stage by

$$TBV_i^{<m-1>} = \left|q_{i-1/2}^{L,<m-1>} - q_{i-1/2}^{R,<m-1>}\right| + \left|q_{i+1/2}^{L,<m-1>} - q_{i+1/2}^{R,<m-1>}\right|, \tag{15}$$

and the TBV for THINC function of β_m by

$$TBV_i^{Tm} = \left|q_{i-1/2}^{L,Tm} - q_{i-1/2}^{R,Tm}\right| + \left|q_{i+1/2}^{L,Tm} - q_{i+1/2}^{R,Tm}\right|. \tag{16}$$

(III-II) Determine the final reconstruction function for cell $\mathcal{I}_i$ using the BVD algorithm as

$$\tilde{q}_i^{<m>}(x) = \begin{cases} \tilde{q}_i^{Tm}; & \text{if } TBV_i^{Tm} < TBV_i^{<m-1>}, \\ \tilde{q}_i^{<m-1>}; & \text{otherwise} \end{cases} . \tag{17}$$

(III-III) Compute the reconstructed values on the left-side of $x_{i+\frac{1}{2}}$ and the right-side of $x_{i-\frac{1}{2}}$ respectively by

$$q^L_{i+\frac{1}{2}} = \tilde{q}_i^{<m>}(x_{i+\frac{1}{2}}) \text{ and } q^R_{i-\frac{1}{2}} = \tilde{q}_i^{<m>}(x_{i-\frac{1}{2}}). \tag{18}$$

In this study, we propose and test fifth order scheme with $\mathrm{P}_4\mathrm{T}_2 - \mathrm{BVD}$, seventh order scheme with $\mathrm{P}_6\mathrm{T}_3 - \mathrm{BVD}$, ninth order scheme with $\mathrm{P}_8\mathrm{T}_3 - \mathrm{BVD}$ and eleventh order scheme with $\mathrm{P}_{10}\mathrm{T}_3 - \mathrm{BVD}$. According to previous study in [27], in all tests of the present study we use $\beta_1 = 1.1$ and $\beta_2 = 1.8$ for $\mathrm{P}_4\mathrm{T}_2 - \mathrm{BVD}$, and $\beta_1 = 1.2, \beta_2 = 1.1$ and $\beta_3 = 1.8$ for $\mathrm{P}_n\mathrm{T}_3 - \mathrm{BVD}(n = 6, 8, 10)$ schemes.

Remark 1. The multi-stage BVD algorithm enables to reinforce the desired numerical properties at different stages. In the intermediate stage ($k = 1, 2, \ldots, m-1$), the oscillation-free property is realized. The final stage ($k = m$) is devised to reduce numerical dissipation to capture sharp discontinuities. The parameter β in the intermediate stage is fixed to realize the non-oscillatory property, while in the final stage the parameter β can be chosen from 1.6 to 2.2. A larger value will result in a sharper discontinuity.

Remark 2. This work provides a new framework to construct high order shock capturing schemes. As shown above, extending the scheme from 7th to 11th order is straightforward by simply applying the high order polynomials of the targeted order as given in (8)-(10). Our numerical experiments shows that higher-order schemes beyond 11th order can be also designed by adding more levels of THINC function and BVD algorithm in the same spirit.

2.2.4. Spectral property

We study the spectral property of the proposed scheme by using approximate dispersion relation (ADR) analysis described in [32]. The numerical dissipation of a scheme can be quantified through the imaginary parts of the modified wavenumber while the numerical dispersion can be quantified with real parts. The spectral properties of different order schemes are shown in Fig. 1 in which the spectral properties of proposed $\mathrm{P}_n\mathrm{T}_m - \mathrm{BVD}$ schemes at different wave numbers are marked by the circles, and the solid lines in the same color represent the spectral properties of the corresponding high order-linear schemes. It can be seen that the proposed schemes have almost the same spectral property as their underlying linear upwind schemes even at high wavenumber band. However, for WENO-type high order schemes, as shown in [32, 18] accuracy is usually undermined at high wavenumber regime although they can recover to their underlying linear scheme at low wavenumber. The reason is that the WENO smoothness indicators

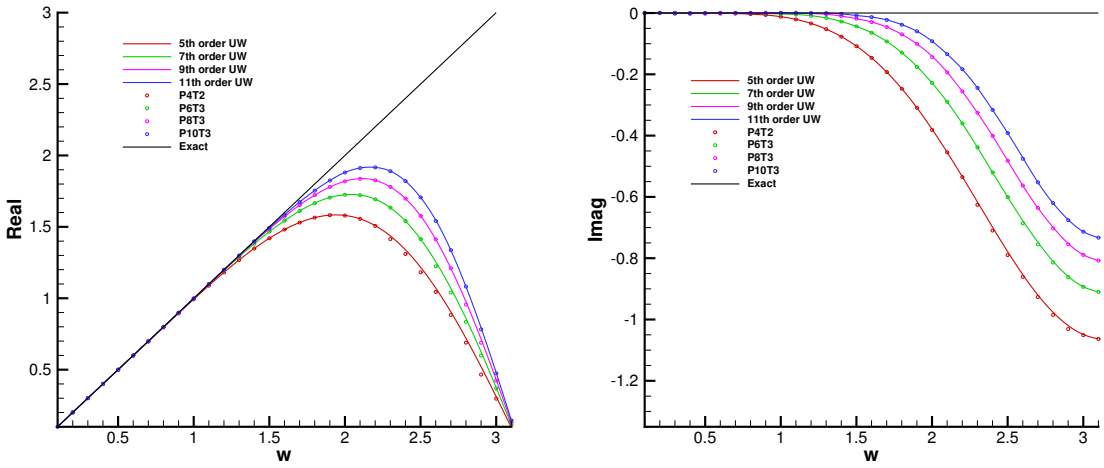

Figure 1: Approximate dispersion and dissipation properties for different order schemes. Real parts of modified wavenumber are shown in the left panel, while imaginary parts are shown in the right. The circles represent the spectral property of proposed P_nT_m – BVD schemes at different wave numbers. The solid lines represent the spectral property of corresponding high order upwind schemes in the same color.

tends to mis-interpret high frequency waves as discontinuities. Contrarily, the proposed P_nT_m – BVD schemes are designed to reduce numerical dissipations, and thus preserve the high-order upwind schemes even in high wavenumber regime, which is hardly realized by any existing high resolution scheme based on limiting projections using nonlinear weighting. It is noteworthy that the ADR analysis method proposed in [32] assumes that the time integration is exact and ignores the influence of time integration scheme. However, according to the works [33, 34, 35, 36] the time integration scheme may have strong effects on the overall scheme capability and may change the numerical dissipation and dispersion property of a scheme. Thus the methods proposed in [33, 36] should be implemented when considering the influence of time schemes.

3. Numerical results

In this section, some numerical experiments are performed as a demonstration of the proposed schemes. Linear advection equations and Euler equation systems will be numerically solved. In all examples, the ratio of specific heats is set to $\gamma = 7/5$ and CFL is set to 0.4. Time discretization schemes of the same order as the space-discretization are applied. In the present work, linear strong-stability-preserving Runge-Kutta algorithms developed in [37] are used. To solve Euler equations, HLLC (Harten, Lax and van Leer with Contact) Riemann solver [38] is used to calculate the numerical fluxes. The reconstruction process is carried out in terms of characteristic variables. To solve multi-dimensional problems, we follow [21] and use simple dimension-wise implementation for 2D Euler equations for the sake of simplicity. As reported in [39], this simple multi-dimensional implementation is able to give adequate

Table 1: Numerical errors and convergence rate for linear advection test. Results are computed by the proposed P_nT_m – BVD schemes.

Schemes	Mesh	L_1 errors	L_1 order	L_∞ errors	L_∞ order
P_4T_2	10	2.493×10^{-1}		3.852×10^{-1}	
	20	1.174×10^{-2}	4.41	1.815×10^{-2}	4.41
	40	3.986×10^{-4}	4.88	6.309×10^{-4}	4.85
	80	1.274×10^{-5}	4.97	2.002×10^{-5}	4.98
P_6T_3	10	8.518×10^{-2}		1.316×10^{-1}	
	20	9.673×10^{-4}	6.46	1.495×10^{-3}	6.46
	40	8.350×10^{-6}	6.86	1.319×10^{-5}	6.82
	80	6.686×10^{-8}	6.96	1.052×10^{-7}	6.97
P_8T_3	10	2.733×10^{-2}		4.223×10^{-2}	
	20	8.216×10^{-5}	8.38	1.269×10^{-4}	8.38
	40	1.816×10^{-7}	8.82	2.870×10^{-7}	8.79
	80	3.659×10^{-10}	8.96	5.756×10^{-10}	8.96
$P_{10}T_3$	10	8.716×10^{-3}		1.347×10^{-2}	
	20	7.132×10^{-6}	10.26	1.102×10^{-5}	10.26
	40	4.041×10^{-9}	10.79	6.388×10^{-9}	10.75
	80	2.051×10^{-12}	10.94	3.227×10^{-12}	10.95

accuracy for problems involving shock waves. It should be noted here that in order to realize truly high-order schemes for multi-dimensional Euler equations, algorithms introduced in [23, 39, 40] should be adopted.

3.1. Accuracy test for advection of one-dimensional sine wave

In order to evaluate the convergence rate of the proposed P_nT_m – BVD schemes, an advection test of smooth profile was conducted on gradually refined grids. The initial smooth distribution was given by

$$q(x) = \sin(2\pi x), \; x \in [-1, 1]. \tag{19}$$

We ran the computation for one period (at $t = 2.0$) and summarized the numerical errors and the convergence rates for P_nT_m – BVD schemes in Table 1. In order to compare with the corresponding high order upwind schemes, we also summarized numerical errors calculated by high order upwind schemes in Table 2. As expected, the proposed P_nT_m – BVD schemes achieved $n + 1$ order convergence rates when grid elements were gradually refined. Importantly, we observed that the L_1 and L_∞ errors from the P_nT_m – BVD schemes were exactly same as those calculated by their corresponding high order linear upwind schemes, which was in line with the conclusion from the spectral property analysis in the previous section. These results confirm that the P_nT_m – BVD schemes are able to recover their underlying high order polynomial interpolations for smooth solutions.

In order to evaluate the computational cost of the proposed schemes, we measure the computational time for the reconstruction process to get interpolated values $q^{L,R}$ with 10^7 cells using one AMD CPU (AMD Ryzen 2970WX 4.20GHz). We also compare the cost with WENOM []. The measurement is summarized in Table 3. It can be seen that the proposed P_nT_m – BVD schemes indeed cost much more than WENO schemes. However, with the order

Table 2: Same as table 1, but by the high-order linear upwind schemes.

Schemes	Mesh	L_1 errors	L_1 order	L_∞ errors	L_∞ order
5th order UW	10	2.493×10^{-1}		3.852×10^{-1}	
	20	1.174×10^{-2}	4.41	1.815×10^{-2}	4.41
	40	3.986×10^{-4}	4.88	6.309×10^{-4}	4.85
	80	1.274×10^{-5}	4.97	2.002×10^{-5}	4.98
7th order UW	10	8.518×10^{-2}		1.316×10^{-1}	
	20	9.673×10^{-4}	6.46	1.495×10^{-3}	6.46
	40	8.350×10^{-6}	6.86	1.319×10^{-5}	6.82
	80	6.686×10^{-8}	6.96	1.052×10^{-7}	6.97
9th order UW	10	2.733×10^{-2}		4.223×10^{-2}	
	20	8.216×10^{-5}	8.38	1.269×10^{-4}	8.38
	40	1.816×10^{-7}	8.82	2.870×10^{-7}	8.79
	80	3.659×10^{-10}	8.96	5.756×10^{-10}	8.96
11th order UW	10	8.716×10^{-3}		1.347×10^{-2}	
	20	7.132×10^{-6}	10.26	1.102×10^{-5}	10.26
	40	4.041×10^{-9}	10.79	6.388×10^{-9}	10.75
	80	2.051×10^{-12}	10.94	3.227×10^{-12}	10.95

Table 3: Numerical errors and convergence rate for linear advection test. Results are computed by the proposed P_nT_m – BVD schemes.

	7th order	9th order	11th order
P_nT_m – BVD	5.25 s	5.33 s	5.41 s
WENOM []	2.48 s	3.25 s	4.12 s

increased, the cost is almost the same for P_nT_m – BVD schemes whereas the cost increases significantly for WENO schemes. To increase the order from seventh- to eleventh-, the P_nT_m – BVD schemes only change the underlying high order interpolations without additional complexity as WENO does.

3.2. Accuracy test for advection of a smooth profile containing critical points

We conducted the accuracy test which was more challenging for numerical schemes to distinguish smooth and non-smooth profiles because the initial distribution contains critical points. It has been reported in [12] that WENO type schemes do not reach their formal order of accuracy at critical points where the high order derivative does not simultaneously vanish. Following [12, 21], the initial condition was given by

$$q(x) = \sin(\pi x - \frac{\sin(\pi x)}{\pi}), \ x \in [-1, 1]. \tag{20}$$

The computation was conducted for ten period ($t = 20$). We summarize the numerical errors L_1 and L_∞ of the proposed P_nT_m – BVD in Table 4 and those of the corresponding upwind schemes in Table 5. It can be seen that the P_nT_m – BVD schemes are capable of achieving their highest possible order of accuracy in the grid refinement tests. Compared with their corresponding upwind schemes, the P_nT_m – BVD schemes almost realize the same L_1 and L_∞ errors, which demonstrates that P_nT_m – BVD schemes restore upwind schemes even at critical points. However, as

Table 4: Numerical errors and convergence rate for advection of a smooth profile containing critical points. Results are calculated by P_nT_m – BVD schemes.

Schemes	Mesh	L_1 errors	L_1 order	L_∞ errors	L_∞ order
P_4T_2	10	1.068×10^{-1}		2.263×10^{-1}	
	20	1.497×10^{-2}	2.83	3.772×10^{-2}	2.58
	40	7.138×10^{-4}	5.13	1.960×10^{-3}	4.27
	80	2.327×10^{-5}	4.94	6.582×10^{-5}	4.90
	160	7.334×10^{-7}	4.99	2.092×10^{-6}	4.98
P_6T_3	10	7.969×10^{-2}		1.306×10^{-1}	
	20	2.539×10^{-3}	4.97	6.565×10^{-3}	4.31
	40	2.610×10^{-5}	6.60	8.020×10^{-5}	6.36
	80	2.135×10^{-7}	6.93	6.654×10^{-7}	6.91
	160	1.691×10^{-9}	6.98	5.269×10^{-9}	6.98
P_8T_3	10	3.702×10^{-2}		6.049×10^{-2}	
	20	5.008×10^{-4}	6.21	1.287×10^{-3}	5.55
	40	1.413×10^{-6}	8.47	4.492×10^{-6}	8.16
	80	2.975×10^{-9}	8.89	9.779×10^{-9}	8.84
	160	5.942×10^{-12}	8.97	1.960×10^{-11}	8.96
$P_{10}T_3$	10	1.449×10^{-2}		2.837×10^{-2}	
	20	1.222×10^{-4}	6.89	3.180×10^{-4}	6.48
	40	9.755×10^{-8}	10.29	3.357×10^{-7}	9.89
	80	5.472×10^{-11}	10.80	1.919×10^{-10}	10.77
	160	4.032×10^{-14}	10.40	1.472×10^{-13}	10.35

shown in [12, 21], it is generally difficult for WENO type schemes to recover their underlying high order upwind schemes particularly around the critical points.

3.3. Advection of complex waves

In order to examine the performance of the proposed scheme in solving profiles of different smoothness, we further simulated the propagation of a complex wave [8]. The initial profile contains both discontinuities and smooth regions with different smoothness, which is given by

$$q(x) = \begin{cases} \frac{1}{6}\left[G(x,\beta,z-\delta) + G(x,\beta,z+\delta) + 4G(x,\beta,z)\right] & \text{if } |x+0.7| \le 0.1, \\ 1 & \text{if } |x+0.3| \le 0.1, \\ 1 - |10(x-0.1)| & \text{if } |x-0.1| \le 0.1, \\ \frac{1}{6}\left[F(x,\alpha,a-\delta) + F(x,\alpha,a+\delta) + 4F(x,\alpha,a)\right] & \text{if } |x-0.5| \le 0.1, \\ 0 & \text{otherwise,} \end{cases} , \tag{21}$$

where functions F and G are defined as

$$G(x,\beta,z) = \exp\left[-\beta(x-z)^2\right], \; F(x,\alpha,a) = \sqrt{\max\left[1-\alpha^2(x-a)^2, 0\right]}, \tag{22}$$

Table 5: Same as table 4, but by high-order linear upwind schemes.

Schemes	Mesh	L_1 errors	L_1 order	L_∞ errors	L_∞ order
5th order UW	10	1.067×10^{-1}		2.265×10^{-1}	
	20	1.793×10^{-2}	2.57	3.874×10^{-2}	2.55
	40	7.138×10^{-4}	4.65	1.960×10^{-3}	4.30
	80	2.327×10^{-5}	4.94	6.582×10^{-5}	4.90
	160	7.334×10^{-7}	4.99	2.092×10^{-6}	4.98
7th order UW	10	7.969×10^{-2}		1.306×10^{-1}	
	20	2.539×10^{-3}	4.97	6.565×10^{-3}	4.31
	40	2.610×10^{-5}	6.60	8.020×10^{-5}	6.36
	80	2.135×10^{-7}	6.93	6.654×10^{-7}	6.91
	160	1.691×10^{-9}	6.98	5.269×10^{-9}	6.98
9th order UW	10	3.702×10^{-2}		6.048×10^{-2}	
	20	5.008×10^{-4}	6.21	1.287×10^{-3}	5.55
	40	1.413×10^{-6}	8.47	4.492×10^{-6}	8.16
	80	2.975×10^{-9}	8.89	9.779×10^{-9}	8.84
	160	5.942×10^{-12}	8.97	1.960×10^{-11}	8.96
11th order UW	10	1.449×10^{-2}		2.837×10^{-2}	
	20	1.222×10^{-4}	6.89	3.180×10^{-4}	6.48
	40	9.755×10^{-8}	10.29	3.357×10^{-7}	9.89
	80	5.472×10^{-11}	10.80	1.919×10^{-10}	10.77
	160	4.032×10^{-14}	10.40	1.472×10^{-13}	10.35

and the coefficients are

$$a = 0.5,\ z = 0.7,\ \delta = 0.005,\ \alpha = 10.0,\ \beta = \log_2\left(36\delta^2\right). \tag{23}$$

The computation was carried out for one period at $t = 2.0$ with a 200-cell mesh. The results calculated by the $\mathrm{P}_n\mathrm{T}_m$ − BVD schemes were presented in Fig. 2. It can be seen that all of schemes are free of visible numerical oscillations and capture sharper discontinuities than conventional high order FVM schemes. With polynomial degree increased, the extreme points of the initial profile are better resolved. It is also noted that $\mathrm{P}_n\mathrm{T}_m$ − BVD schemes produce almost same results for the discontinuity which is resolved by only four cells. Because the BVD algorithm can properly choose THINC reconstruction function across discontinuities, increasing order is only effective to the resolution of smooth regions.

3.4. Sod's problem

As one of widely used benchmark tests for shock-capturing schemes, the Sod's problem was employed to test the performance of present schemes in capturing the shock front, contact discontinuity, as well as the expansion wave. The initial distribution on computational domain $[0, 1]$ was specified as [41]

$$(\rho_0,\ u_0,\ p_0) = \begin{cases} (1,\ 0,\ 1) & 0 \le x \le 0.5 \\ (0.125,\ 0,\ 0.1) & \text{otherwise} \end{cases}. \tag{24}$$

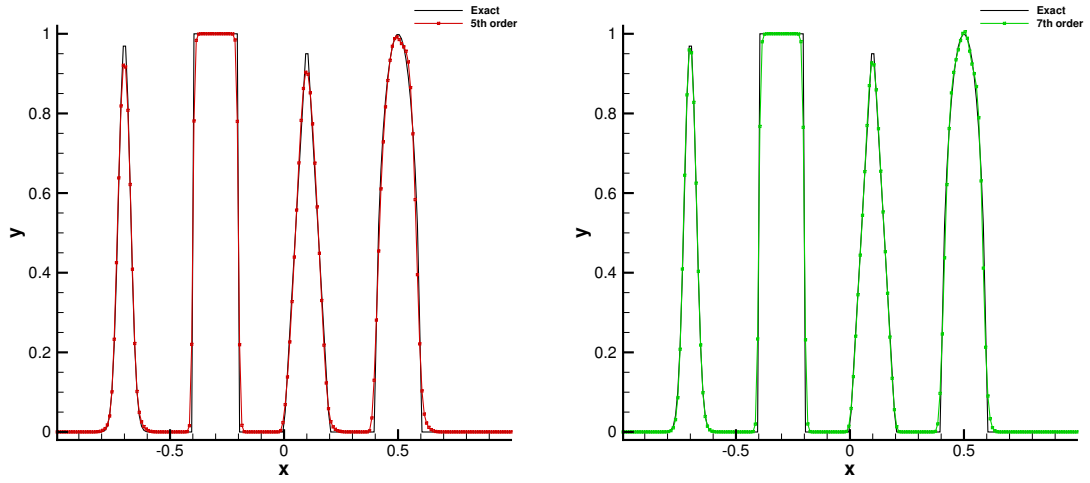

(a) P_4T_2

(b) P_6T_3

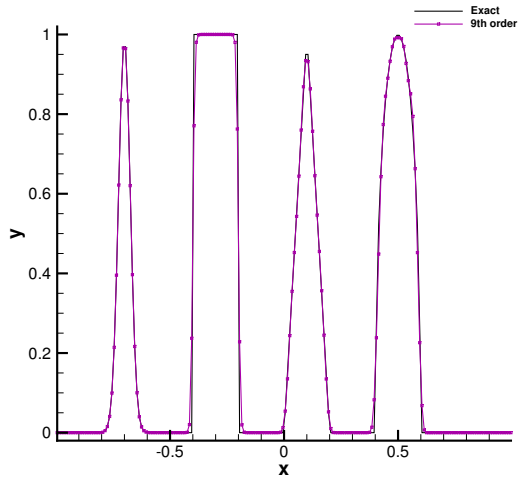

(c) P_8T_3

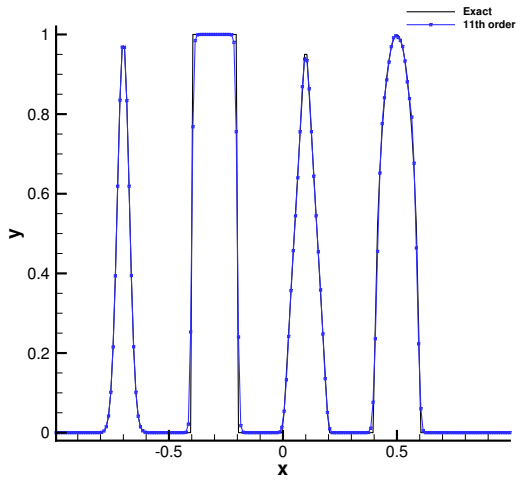

(d) $P_{10}T_3$

Figure 2: Numerical results for advection of complex waves. The numerical solutions at $t = 2.0$ with 200 mesh cells are presented.

The computation was carried out on a mesh of 100 uniform cells up to $t = 0.25$. The numerical results calculated from the proposed scheme were shown in Fig. 3 for density fields. From the results, we observe that $\mathrm{P}_n\mathrm{T}_m$ − BVD schemes can solve the contact discontinuity without obvious numerical oscillations. Compared with the results produced by other high order shock-capturing schemes [8, 12, 13, 14, 18, 19], the results of the proposed schemes are among the best with the jump contact resolved within only two cells. We also observe that $\mathrm{P}_n\mathrm{T}_m$ − BVD schemes of different orders produce similar results across the contact where the THINC function is selected by the BVD algorithm. We also mark the cells where THINC function with $\beta = 1.8$ is selected in the Fig. 3. It can be seen the BVD algorithm is able to select the jump-like THINC function across discontinuities.

3.5. Lax's problem

Shock schemes should be able to deal with the possibility of existing strong discontinuities such as shock waves and detonation waves [42, 43]. In this subsection, we solved the Lax problem [5] in this subsection. The initial condition is given by

$$(\rho_0,\ u_0,\ p_0) = \begin{cases} (0.445,\ 0.698,\ 3.528) & 0 \le x \le 0.5 \\ (0.5,\ 0.0,\ 0.571) & \text{otherwise} \end{cases}. \tag{25}$$

With the same number of cells as in the previous test case, we got the numerical results at $t = 0.16$. The density field is plotted presented in Fig. 4. Obviously, the proposed $\mathrm{P}_n\mathrm{T}_m$−BVD schemes obtain accurate solutions without numerical oscillations. Again, the BVD algorithm chooses the THINC function across the discontinuity, which produces similar results among $\mathrm{P}_n\mathrm{T}_m$−BVD schemes of different order. Compared with numerical results using very high order WENO schemes (see the Fig. 8 in [21]), the present results are one of best.

3.6. Shock density wave interaction problem

Here, we simulate the case proposed in [6] containing shocks and complex smooth flow features. The initial condition is set as

$$(\rho_0,\ u_0,\ p_0) = \begin{cases} (3.857148,\ 2.629369,\ 10.333333), & \text{if } 0 \le x \le 0.1, \\ (1 + 0.2\sin(50x - 25),\ 0,\ 1), & \text{otherwise.} \end{cases} \tag{26}$$

The numerical solutions at $t = 0.18$ computed on 200 are shown in Fig. 5, where the reference solution plotted by the solid line is computed by the classical 5th-order WENO scheme with 2000 mesh cells. With the order increased, the peak of the waves is resolved more accurately.

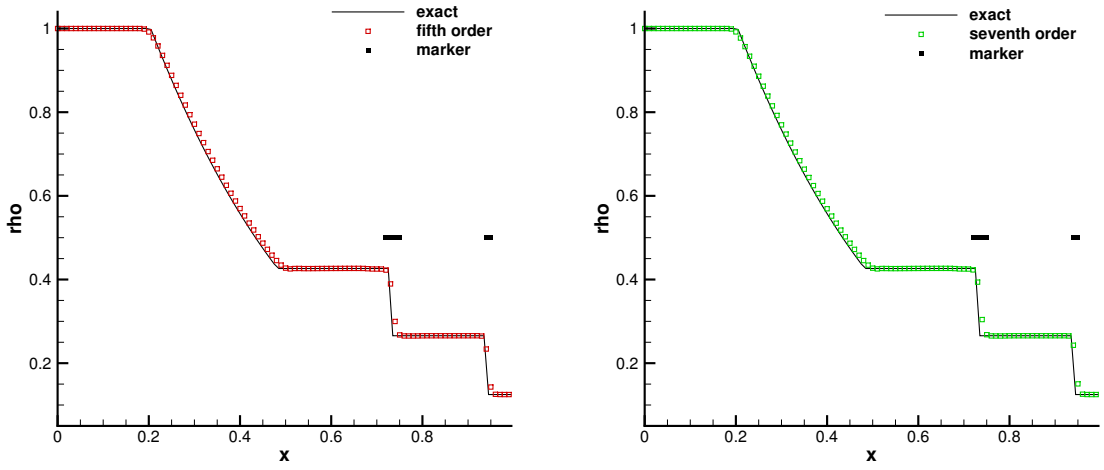

(a) P_4T_2

(b) P_6T_3

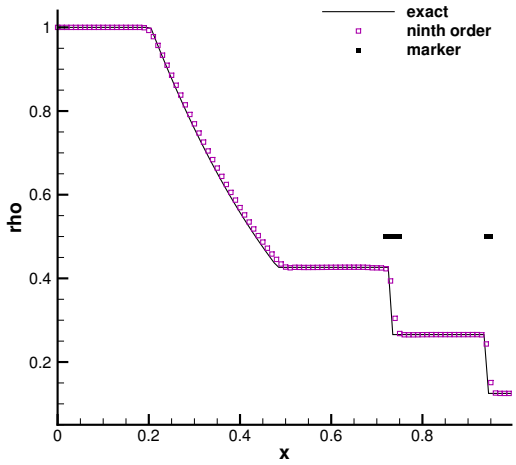

(c) P_8T_3

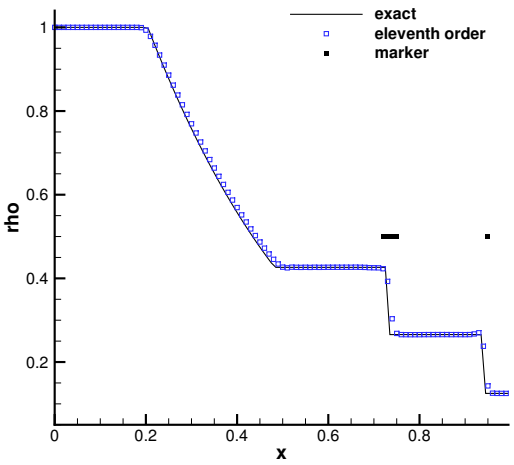

(d) $P_{10}T_3$

Figure 3: Numerical results of Sod's problem for density field at $t = 0.25$ with 100 cells. The cells where THINC function with $\beta = 1.8$ is selected are marked with solid black.

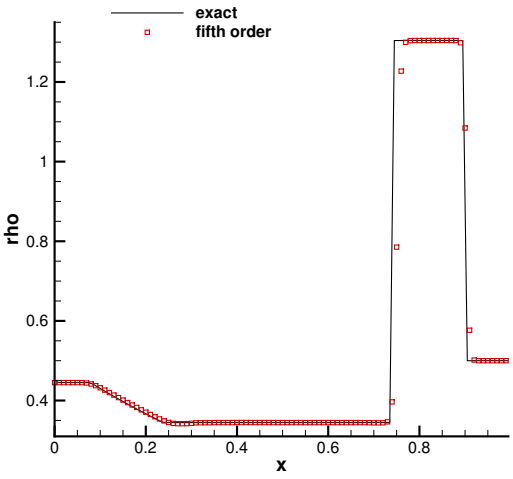

(a) P_4T_2

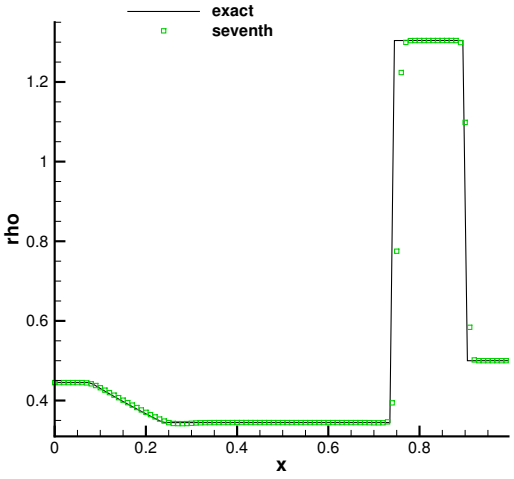

(b) P_6T_3

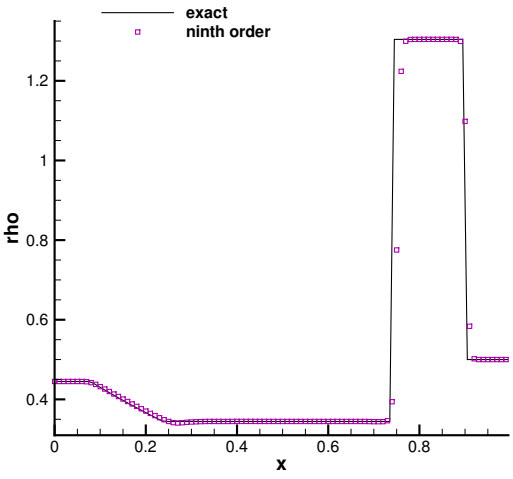

(c) P_8T_3

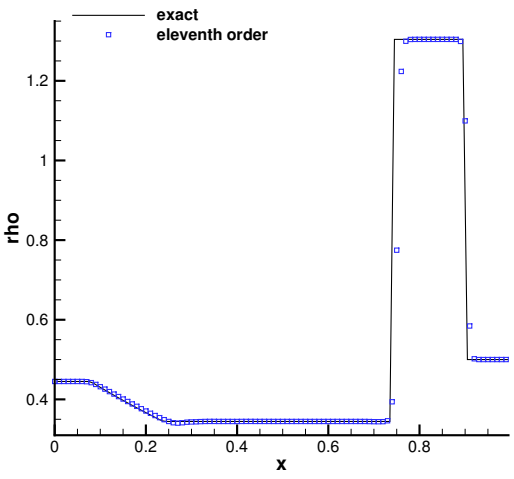

(d) $P_{10}T_3$

Figure 4: Numerical results of Lax's problem for density field at time $t = 0.16$ with 100 cells.

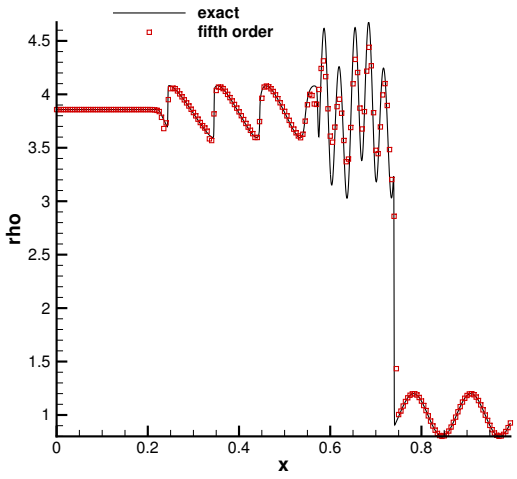

(a) P_4T_2

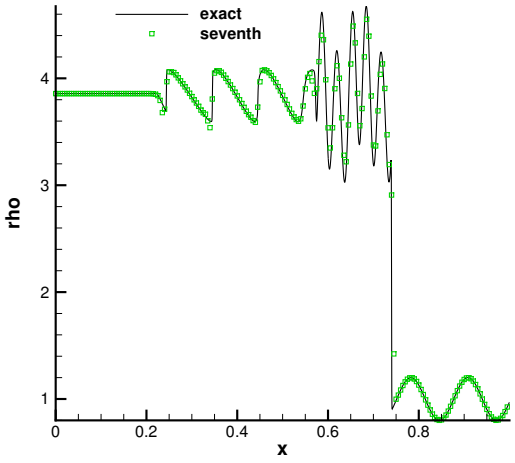

(b) P_6T_3

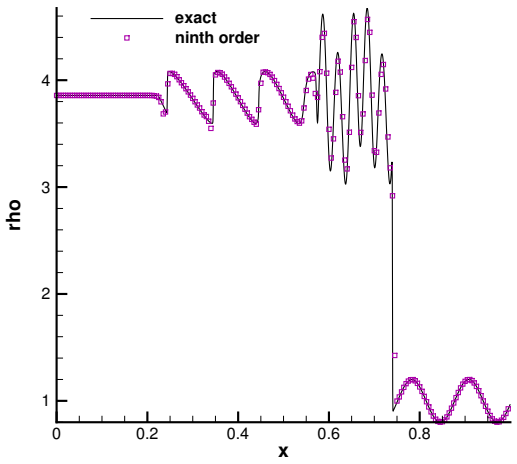

(c) P_8T_3

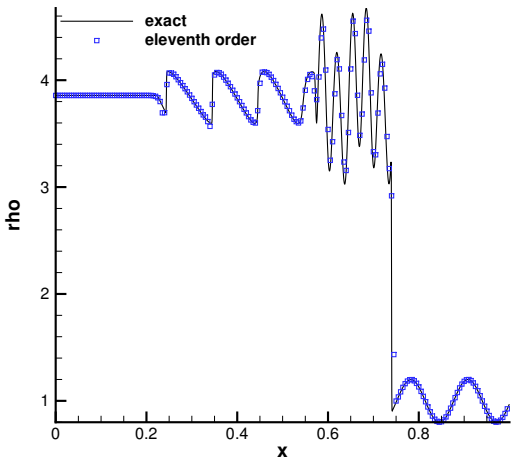

(d) $P_{10}T_3$

Figure 5: Numerical results of shock/density wave interaction problem. The results with 200 mesh cells are shown.

3.7. Two interacting blast waves

Interactive blast waves involving multiple interactions of strong shocks and rarefaction waves has been introduced in [44]. The initial distribution is given by

$$(\rho_0,\ u_0,\ p_0) = \begin{cases} (1,\ 0,\ 1000), & \text{if } 0 \le x < 0.1, \\ (1,\ 0,\ 0.01), & \text{if } 0.1 \le x < 0.9, \\ (1,\ 0,\ 100), & \text{if } 0.9 \le x < 1. \end{cases} \tag{27}$$

Reflective boundary conditions are imposed at the two ends of computational domain. Two blast waves are generated by the initial jumps and then evolve, associated with violent interactions among different flow structures. We used 400 mesh cells as used in most literature for this test problem, and depict the numerical density at time $t = 0.038$ in Fig. 6 against a reference solution obtained with WENO scheme using a very fine mesh. The solution produced by very high order WENO type schemes on 400-cell mesh can be found in the Fig. 14 [21] where solutions are smeared significantly. On the contrary, the proposed $\mathrm{P}_n\mathrm{T}_m - \mathrm{BVD}$ schemes show overall better resolution and can capture the left-most contact discontinuity with only three points.

3.8. 2D Riemann problems

Two-dimensional Riemann problems which have been proposed and extensively studied in [45, 46] are employed to show that the extension of the new scheme to two dimensions can produce accurate, robust and non-oscillatory solutions for compressible flows of complex structures. With different initial configurations made of 2×2 constant states, the 2D Riemann problems are usually employed as benchmark tests to examine the behavior of numerical schemes. It has been noted that Kelvin-Helmholtz instability tends to develop along the interfaces between those states. As reported in [47, 21, 48, 49, 50, 51], capturing the discontinuities with adequate sharpness between different states is very crucial for the development of Kelvin-Helmholtz instability and small-scale structures which can only be generated by fine enough grids or very high order schemes.

We used a computational domain of $[-0.5, 0.5] \times [-0.5, 0.5]$, and set the initial conditions as follows,

$$(\rho_0,\ u_0,\ v_0,\ p_0) = \begin{cases} (1.0,\ -0.6259,\ 0.1,\ 1.0) & x \le 0.0,\ y \ge 0.0 \\ (0.8,\ 0.1,\ 0.1,\ 1.0) & x < 0.0,\ y < 0.0 \\ (0.5197,\ 0.1,\ 0.1,\ 0.4) & x > 0.0,\ y > 0.0 \\ (1.0,\ 0.1,\ -0.6259,\ 1.0) & x > 0.0,\ y < 0.0 \end{cases}. \tag{28}$$

A uniform grid made of 800×800 cells was employed in all calculations. The numerical results solved by the proposed schemes were presented in Fig. 7. Compared with the reference solution which can be found in [51], the new schemes resolve correctly the major flow features. Moreover, the new schemes obtain small-scale structures

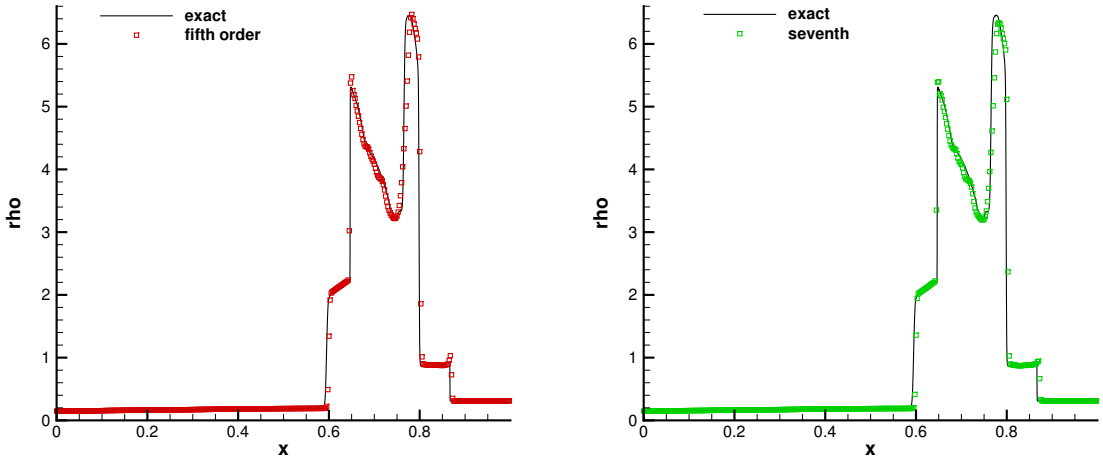

(a) P_4T_2

(b) P_6T_3

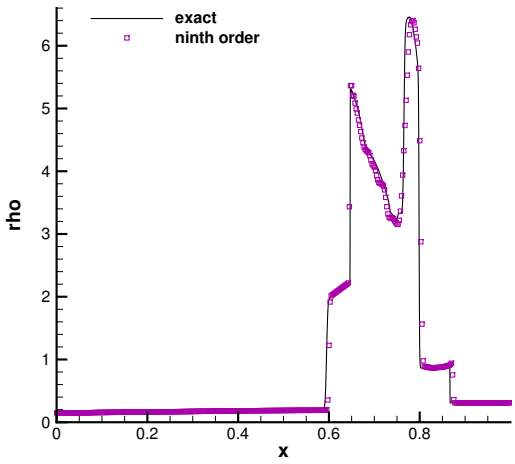

(c) P_8T_3

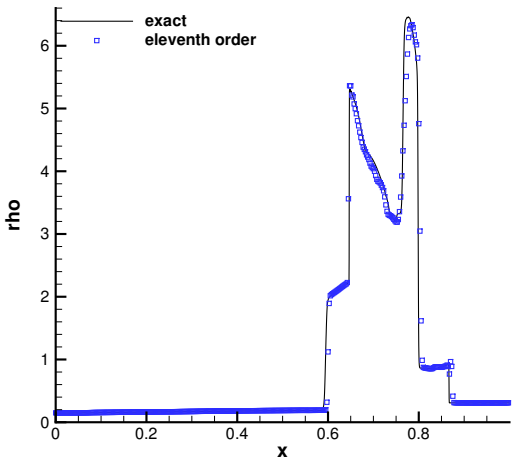

(d) $P_{10}T_3$

Figure 6: Numerical results of two interacting blast waves problem for density field at t = 0.038 with 400 cells.

caused by Kelvin-Helmholtz instability, which is a challenging for other high order schemes as reported in [51]. It can be also observed that the vortical structures become richer as the order of schemes increases, which agrees with the observations reported in [21] that the number of vortices depends on the order of the scheme and mesh resolution.

3.9. Double Mach Reflection

As a 2D problems involving strong shocks and vortical structures, the double Mach reflection generated by a Mach 10 hypersonic propagating planar shock reflected by a 30° ramp [52] is simulated here to evaluate the performance of the new schemes. This test has been adopted widely to assess the ability of a numerical scheme to capture accurately both the strong reflected shocks as well as the small-scale structures in the re-circulation zone. Without exact solution, the numerical dissipation of a numerical scheme can be visually assessed by the richness of vortex structures resulted from Kelvin-Helmholtz instabilities along the slip line in the re-circulation zone. The numerical schemes with large numerical viscosity tend to smear out these structures. In our test, the computational domain was $[0, 3.2] \times [0, 1]$. A right-moving Mach 10 shock was imposed with 60° angle relative to x-axis. The solution was computed up to time $t = 0.2$ with a grid resolution of $\Delta x = \Delta y = \frac{1}{200}$. The numerical results calculated by the proposed schemes of different order are shown in Fig. 8. Despite of the existence of strong shock waves, all $\mathrm{P}_n\mathrm{T}_m - \mathrm{BVD}$ schemes successfully reproduce essentially non-oscillatory numerical results. The solution quality of the present numerical results is competitive to other advanced high-resolution schemes, such as [52, 18]. Of particular importance, the proposed schemes obtain well developed vortex structures along the slip line, which demonstrates the robust and low-dissipation property of the schemes.

3.10. 2D shock-entropy wave interaction problem

In this subsection, we simulated the 2D shock entropy wave interaction problem which is usually used as one of simplest models for flow interactions involved in compressible turbulence. Similar to that specified in [16], the initial condition is given by

$$(\rho_0,\ u_0,\ v_0,\ p_0) = \begin{cases} (3.85714,\ 2.62936,\ 0,\ 10.33333)\,, & \text{if } x \le -4, \\ (1 + 0.2\sin(14x\cos\theta + 14y\sin\theta)\,,\ 0,\ 0,\ 1)\,, & \text{otherwise.} \end{cases} \tag{29}$$

with $\theta = \pi/6$ which is the angle of the initial sine wave front with respect to the x axis. The computational domain is $[-5, 5] \times [-1, 1]$ with periodic conditions in y direction. The mesh size of $h = 1/40$ was used for simulation. We conducted the computation until $t = 1.8$. The numerical results calculated by $\mathrm{P}_n\mathrm{T}_m - \mathrm{BVD}$ schemes of different orders are presented in Fig. 9. We also calculated the reference solution by the original WENO scheme with a finer mesh in Fig. 10(a). With the order increased, it can be seen that the high-frequency density field is better resolved. We plot the density distribution along $y = 0.0$ cross section in Fig. 10(b). Similar to the 1D case, with a higher order

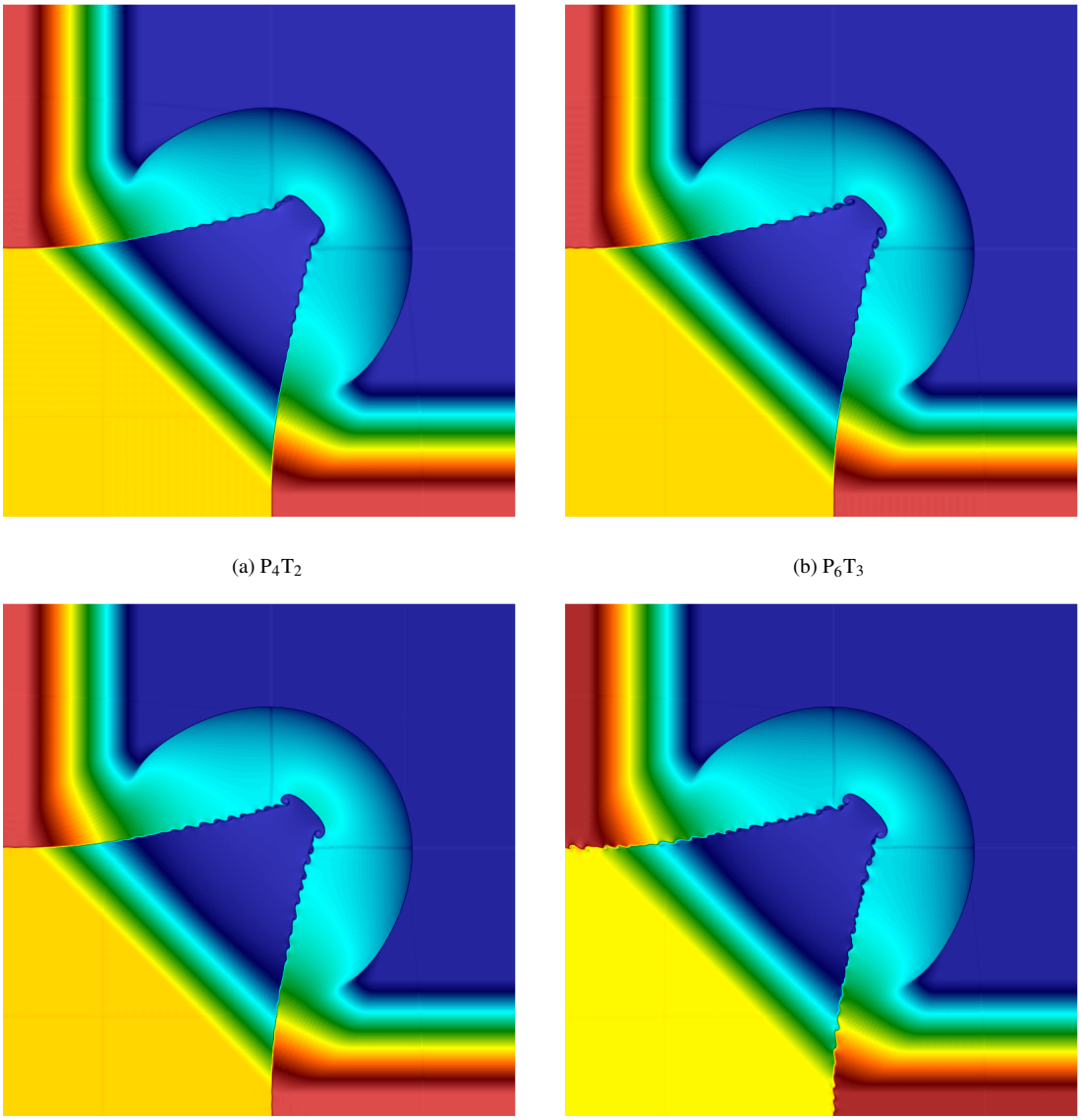

(a) P_4T_2 (b) P_6T_3

(c) P_8T_3 (d) $P_{10}T_3$

Figure 7: Numerical solutions of density field for 2D Riemann problems.

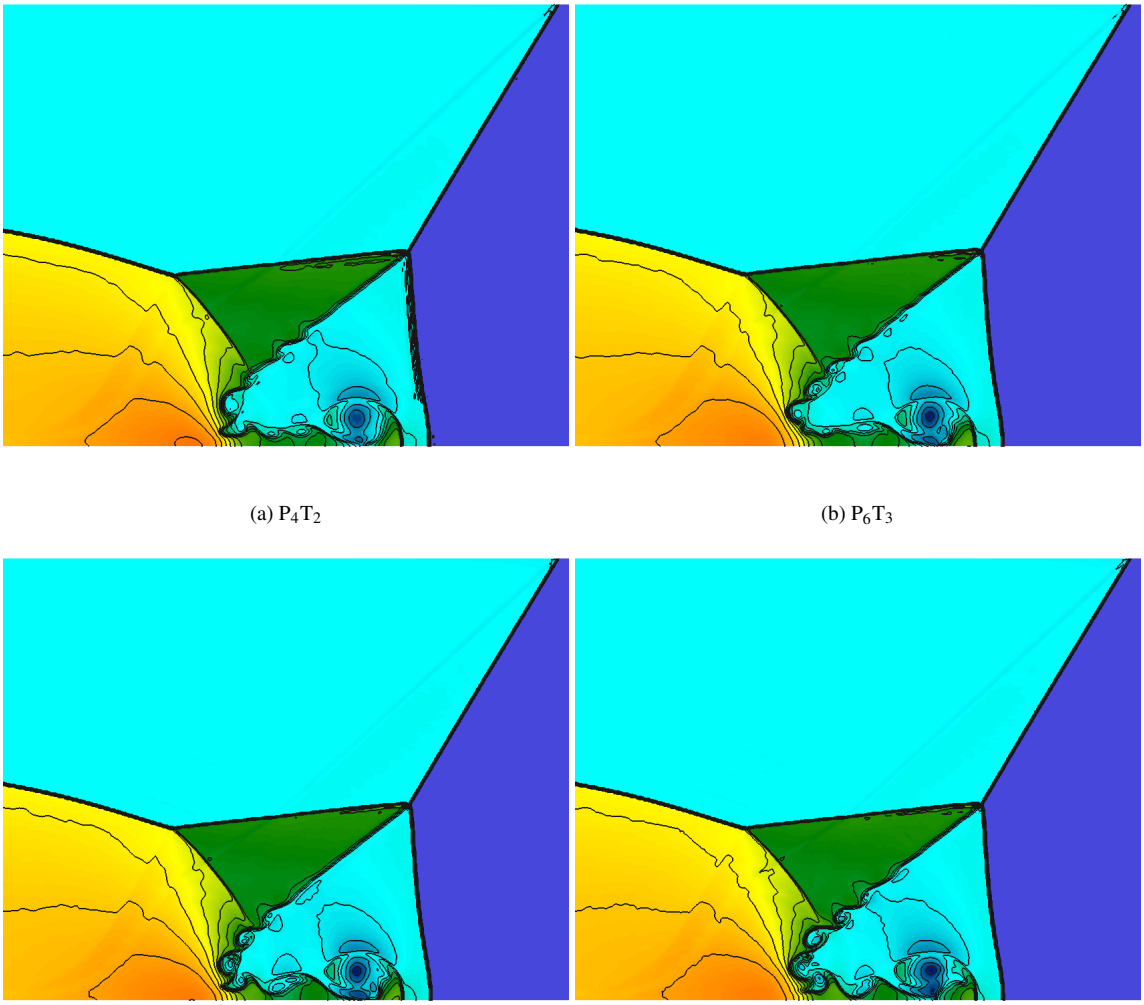

(a) P_4T_2 (b) P_6T_3

(c) P_8T_3 (d) $P_{10}T_3$

Figure 8: Numerical solutions for double Mach 10 refection problem. The figures show the enlarged re-circulation zone.

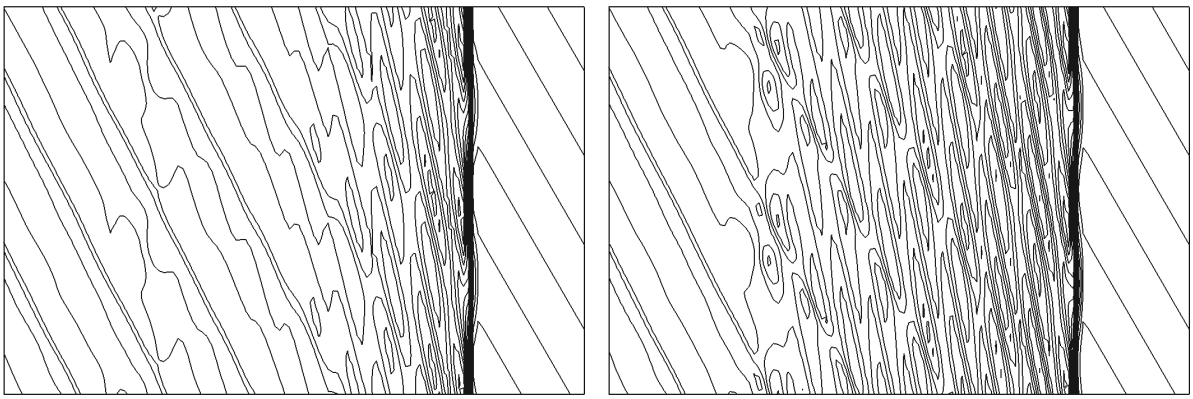

(a) P_4T_2 (b) P_6T_3

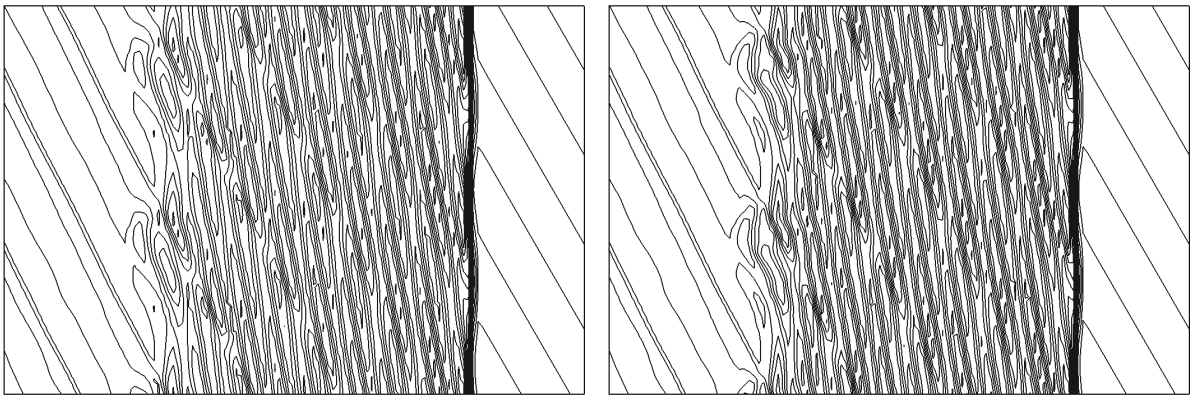

(c) P_8T_3 (d) $P_{10}T_3$

Figure 9: Numerical solution for the 2D shock-entropy wave interaction problem. The density contours calculated by P_nT_m − BVD schemes of different orders are presented.

reconstruction, the scheme captures the extreme points more accurately with less numerical dissipation. From this case, it is obviously that very high order schemes are preferred to simulate problems involving small-scale structures which are common in shock-turbulence problems.

3.11. Shock vortex interaction

In this subsection, a shock-vortex interaction test is simulated. This problem is originally proposed in [53] and reported in [47]. As stated in [47], this test is considered as a more realistic benchmark test for evaluating high order numerical schemes since it involves smooth vortical flow structures and discontinuous shock waves. The computation domain is $[0, 2] \times [0, 1]$ with mesh size of $h = 1/100$. The reflection boundary condition is prescribed on the top and bottom boundaries. A stationary Mach 1.5 planar shock normal to x direction and a vortex are placed at $x = 0.5$ and

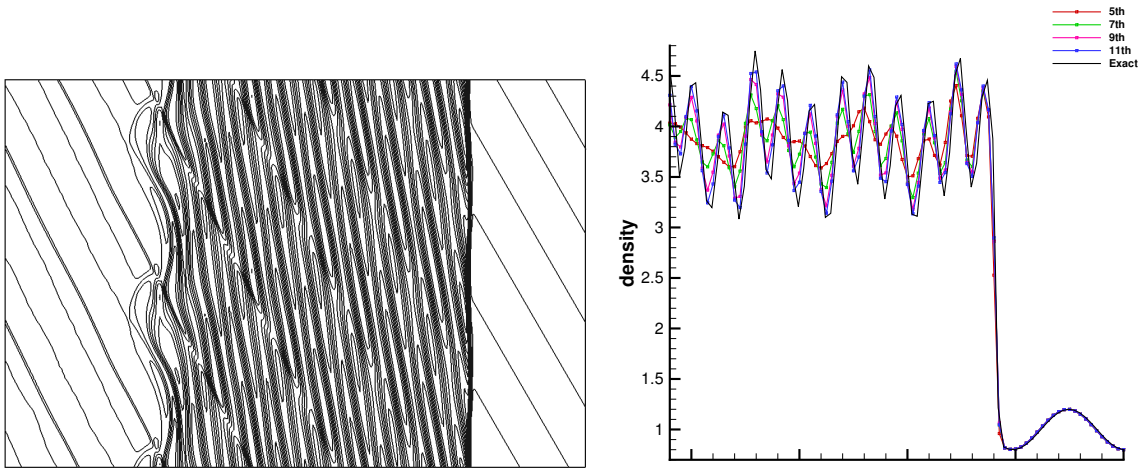

(a) Reference

(b) Density distribution at $y = 0$

Figure 10: Reference solution for the 2D shock-entropy wave interaction problem (left panel) and the density distribution along y=0 cross section by different order schemes (right panel).

$(x_c, y_c) = (0.25, 0.5)$ respectively. The distribution of angular velocity inside the vortex is calculated as

$$u_\phi = \begin{cases} u_m \dfrac{r}{a} & \text{for } r \le a \\ u_m \dfrac{a}{a^2 - b^2}(r - \dfrac{b^2}{r}) & \text{for } a \le r \le b \\ 0 & \text{otherwise} \end{cases}, \tag{30}$$

where $r = \sqrt{(x - x_c)^2 + (y - y_c)^2}$. The strength of the vortex is described with $M_V = u_m/c_0$ in which c_0 is the sound speed in upstream of the shock. The specific values of these parameters are $M_V = 0.9$, $a = 0.075$ and $b = 0.175$.

The results of density gradient field are presented in the Fig. 11. All schemes produce essentially non-oscillatory results. With order increased, the vortex after interacting with the shock begins to split, which agrees well with the numerical simulation in Fig. 9 of [54]. From the observation in [54], the splitting of the vortex can only be resolved with less dissipative scheme. It verifies hence that the high order schemes presented in this paper are able to obtain high resolution results for problems involving shock waves and smooth vortical features.

4. Concluding remarks

In this study, a new type of very high order reconstruction schemes, so-called $\mathrm{P}_n\mathrm{T}_m$ − BVD, is proposed in the finite volume framework. The new scheme hybridizes polynomial of degree n and THINC function with m-level steepness. The effective reconstruction function in each cell is determined by the BVD algorithm which minimizes the numerical dissipation. High order accuracy can be realized in an efficient and straightforward way by directly

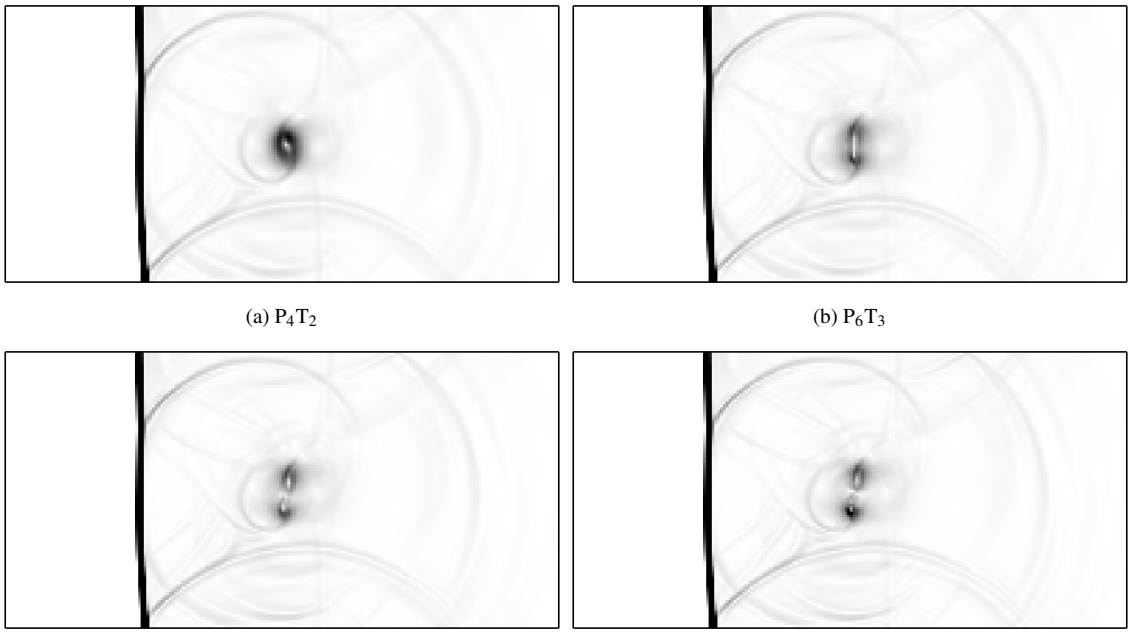

(a) P_4T_2 (b) P_6T_3

(c) P_8T_3 (d) $P_{10}T_3$

Figure 11: Numerical Schlieren images obtained by the proposed P_nT_m − BVD schemes of different orders. The computation was conducted with a mesh spacing of $h = 1/100$.

increasing the degree of polynomial. We extend the new scheme to eleventh order in present study. The spectral analysis and numerical tests show that the P_nT_m − BVD schemes can retrieve the underlying low-dissipation linear schemes over all wave numbers for smooth solutions. The benchmark tests verify that the proposed schemes can capture sharp discontinuities with numerical oscillations effectively suppressed. Moreover, as the order is increased, small-scale flow features can be resolved with much less numerical dissipation. Thus this work provides an innovative and practical alternative approach for spatial reconstructions of very high order for finite volume method to solve hyperbolic conservative systems that contain discontinuous and smooth solutions of various scales. In future works, we will apply the proposed schemes to complex systems including acoustic waves, turbulence and moving interfaces. For example, one of our recent work [55] shows the P_nT_m – BVD is able to achieve promising results for compressible turbulence flow.

Acknowledgment

This work was supported in part by the fund from JSPS (Japan Society for the Promotion of Science) under Grant Nos. 15H03916, 17K18838 and 18H01366. The career of Xi Deng at M2P2 was made possible by Labex MEC (ANR-10-LABX-0092) and the A*MIDEX project (ANR-11-IDEX-0001-02). Especially, Xi Deng would like to express gratitude to Dr. Pierre Boivin who supported his life and research in France.

References

[1] A. Harten, High resolution schemes for hyperbolic conservation laws, J. Comput. Phys. 49 (1983) 357-393.
[2] B. Van Leer, Towards the ultimate conservative difference scheme. V. A second-order sequel to Godunov's method, J. Comput. Phys. 32 (1979) 101-136.
[3] A. Harten, S. Osher, Uniformly high-order accurate non-oscillatory schemes, IMRC Technical Summary Rept. 2823, Univ. of Wisconsin, Madison, WI, May 1985.
[4] A. Harten, B. Engquist, S. Osher, S. Chakravarthy, Uniformly high order accurate essentially non-oscillatory schemes III, J. Comput. Phys. 71 (1987) 231-323.
[5] C.W. Shu, S. Osher, Efficient implementation of essentially non-oscillatory shock capturing schemes, J. Comput. Phys. 77 (1988) 439-471.
[6] C.W. Shu, S. Osher, Efficient implementation of essentially non-oscillatory shock capturing schemes,II, J. Comput. Phys. 83 (1989) 32-78.
[7] X.D. Liu, S. Osher, T. Chan, Weighted essentially non-oscillatory schemes, J. Comput. Phys. 115 (1994) 200-212.
[8] G.S. Jiang, C.-W. Shu, Efficient implementation of weighted ENO schemes, J. Comput. Phys. 126 (1996) 202-228.
[9] S. Clain, S. Diot, Loubàere, A high-order finite volume method for systems of conservation laws-multi-dimensional optimal order detection (MOOD), J. Comput. Phys. 230 (2011) 4028-4050.
[10] S. Diot, S. Clain, Loubàere, Improved detection criteria for the multi-dimensional optimal order detection (MOOD) on unstructured meshes with very high-order polynomials, Comput. & Fluids 64 (2012) 43-63 (2012).
[11] S. Diot, Loubàere, S. Clain, The MOOD method in the three-dimensional case: very-high-order finite volume method for hyperbolic systems. Int. J. Numer. Methods Fluids 73(2013) 362-392.
[12] A.K. Henrick, T.D. Aslam, J.M. Powers, Mapped weighted essentially non-oscillatory schemes: achieving optimal order near critical points, J. Comput. Phys. 207 (2005) 542-567.
[13] R. Borges, M. Carmona, B. Costa, W.S. Don, An improved weighted essentially non-oscillatory scheme for hyperbolic conservation laws, J. Comput. Phys. 227 (2008) 3191-3211.
[14] Y.Ha, C.H. Kim, Y.J. Lee, J. Yoon, An improved weighted essentially non-oscillatory scheme with a new smoothness indicator, J. Comput. Phys. 232 (2013) 68-86.
[15] P.Fan, Y. Shen, B. Tian, C. Yang, A new smoothness indicator for improving the weighted essentially non-oscillatory scheme, J. Comput. Phys. 269 (2014) 329-354.
[16] F. Acker, R. Borges, B. Costa, An improved WENO-Z scheme, J. Comput. Phys. 313 (2016) 726-753.
[17] X.Y. Hu, Q. Wang, N.A. Adams, An adaptive central-upwind weighted essentially non-oscillatory scheme, J. Comput. Phys. 229 (2010) 8952-8965.
[18] L. Fu, X.Y. Hu, N.A. Adams, A family of high-order targeted ENO schemes for compressible-fluid simulations, J. Comput. Phys. 305 (2016) 333-359.
[19] B.S. van Lith, J.H. ten Thije Boonkkamp, W.L. IJzerman, Embedded WENO: A design strategy to improve existing WENO schemes, J. Comput. Phys. 330 (2017) 529-549.
[20] D.S. Balsara, C.W. Shu, Monotonicity preserving WENO schemes with increasingly high-order of accuracy, J. Comput. Phys. 160 (2000) 405?452.
[21] G.A. Gerolymos, D. Sénéchal, I.Vallet, Very-high-order WENO schemes, J. Comput. Phys. 228 (2009) 8481-8524.
[22] D.S. Balsara, S. Garain, C.W. Shu, An efficient class of WENO schemes with adaptive order, J. Comput. Phys. 326 (2016) 780-804.
[23] V.A. Titarev, E.F. Toro, Finite-volume WENO schemes for three-dimensional conservation laws, J. Comput. Phys. 201 (2004) 238-260.
[24] Z. Sun, S. Inaba, F. Xiao, Boundary Variation Diminishing (BVD) reconstruction: A new approach to improve Godunov schemes, J. Comput. Phys. 322 (2016) 309-325.
[25] X. Deng, S. Inaba, B. Xie, K.M. Shyue, F. Xiao, High fidelity discontinuity-resolving reconstruction for compressible multiphase flows with moving interfaces, J. Comput. Phys. 371 (2018) 945-966.
[26] X. Deng, B. Xie, F. Xiao, H. Teng, New Accurate and Efficient Method for Stiff Detonation Capturing, AIAA J. (2018) 1-15.
[27] X. Deng, B. Xie, R. Loubère, Y. Shimizu, F. Xiao, Limiter-free discontinuity-capturing scheme for compressible gas dynamics with reactive fronts, Comput. Fluids, 171 (2018) 1-14.
[28] X. Deng, Y. Shimizu, F. Xiao, A fifth-order shock capturing scheme with two-stage boundary variation diminishing algorithm, J. Comput. Phys. 386 (2019) 323-349.
[29] D.S. Balsara, C.W. Shu, Monotonicity prserving WENO schemes with increasingly high-order of accuracy, J. Comput. Phys. 160 (2000) 405-452.
[30] F. Xiao, S. Ii, C. Chen, Revisit to the THINC scheme: a simple algebraic VOF algorithm, J. Comput. Phys. 230 (2011) 7086-7092.
[31] F. Xiao, Y. Honma, T. Kono, A simple algebraic interface capturing scheme using hyperbolic tangent function, Int. J. Numer. Methods Fluids 48 (2005) 1023-1040.
[32] S. Pirozzoli, On the spectral properties of shock-capturing schemes, J. Comput. Phys. 219 (2006) 489-497.
[33] Y.G. Bhumkar, T.W.H. Sheu, T.K. Sengupta, A dispersion relation preserving optimized upwind compact difference scheme for high accuracy flow simulations, J. Comput. Phys. 278 (2014) 378-399.
[34] R. Bose, T.K. Sengupta, Analysis and design of a new dispersion relation preserving alternate direction bidiagonal compact scheme, J. Sci. Comput. 61 (2014) 1-28.
[35] T.K. Sengupta, High Accuracy Computing Methods: Fluid Flows and Wave Phenomenon, Cambridge Univ. Press, USA, 2013.
[36] J.Vanharen, G.Puigt, X.Vasseur, J.F.Boussuge, P.Sagaut, Revisiting the spectral analysis for high-order spectral discontinuous methods, J. Comput. Phys. 337 (2017) 379-402.
[37] S. Gottlieb, L.A.J. Gottlieb, Strong stability preserving properties of Runge-Kutta time discretization methods for linear constant coefficient operators, J. Sci. Comput. 18 (1) (2003) 83-109.
[38] E.F. Toro, 2013. Riemann solvers and numerical methods for fluid dynamics: a practical introduction. Springer Science & Business Media.

[39] R. Zhang, M. Zhang, C.W. Shu, On the order of accuracy and numerical performance of two classes of finite volume WENO schemes, Commun. Comput. Phys. 9 (2011) 807-827.
[40] P. Buchmüller, C. Helzel, Improved accuracy of high-order WENO finite volume methods on Cartesian grids, J. Sci. Comput. 61 (2014) 343-368.
[41] G.A. Sod, A survey of several finite difference methods for systems of nonlinear hyperbolic conservation laws, J. Comput. Phys. 27 (1978) 1-31.
[42] H.H. Teng , Z.L. Jiang , On the transition pattern of the oblique detonation structure, J. Fluid Mech. 713 (2012) 659-669.
[43] H.H. Teng , Z.L. Jiang , H.D. Ng , Numerical study on unstable surfaces of oblique detonations, J. Fluid Mech. 744 (2014) 111-128 .
[44] P. Woodward, P. Colella, The numerical simulation of two-dimensional fluid flow with strong shocks, J. Comput. Phys. 54 (1984) 115-173.
[45] C.W. Schulz-Rinne, Classification of the Riemann problem for two-dimensional gas dynamics, SIAM J. Math. Anal 24 (1993) 76-88.
[46] A. Kurganov, E. Tadmor, Solution of two-dimensional Riemann problems for gas dynamics without Riemann problem solvers, Numer. Methods Partial Differential Equations 18 (2002) 584-608.
[47] M. Dumbser, O. Zanotti, R. Loubère, S. Diot, A posteriori subcell limiting of the discontinuous Galerkin finite element method for hyperbolic conservation laws, J. Comput. Phys. 278 (2014) 47-75.
[48] Y. Ha, C.H. Kim, Y.J. Lee, J. Yoon, An improved weighted essentially non-oscillatory scheme with a new smoothness indicator, J. Comput. Phys. 232 (2013) 68-86.
[49] P. Buchmüller, C. Helzel, Improved accuracy of high-order WENO finite volume methods on Cartesian grids, J. Sci. Comput. 61 (2014) 343-368.
[50] R. Abedian, H. Adibi, M. Dehghan, A high-order symmetrical weighted hybrid ENO-flux limiter scheme for hyperbolic conservation laws, Comput. Phys. Comm. 185 (2014) 106-127.
[51] C.Y. Jung, T.B. Nguyen, Fine structures for the solutions of the two-dimensional Riemann problems by high-order WENO schemes, Adv. Comput. Math. (2017) 1-28.
[52] P. Woodward, P. Colella, The numerical simulation of two-dimensional fluid flow with strong shocks, J. Comput. Phys. 54 (1984) 115-173.
[53] A. Rault, G. Chiavassa, R. Donat, Shock-vortex interactions at high Mach numbers, J. Sci. Comput. 19 (2003) 347-371
[54] M. Dumbser, M. Käser, V.A. Titarev, E.F. Toro, Quadrature-free non-oscillatory finite volume schemes on unstructured meshes for nonlinear hyperbolic systems, J. Comput. Phys. 226 (2007) 204-243.
[55] X. Deng, Z.H. Jiang, Y. Chao, F. Xiao, Implicit large eddy simulation of compressible turbulence flow with PnTm-BVD scheme, Appl. Math. Model. 77 (2020) 17-31.